NASA Technical Memorandum 103944

Assessment of Higher Order Turbulence Models for Complex Two- and Three-Dimensional Flowfields

Florian R. Menter, Eloret Institute, Palo Alto, California

September 1992

National Aeronautics and
Space Administration

Ames Research Center
Moffett Field, California 94035-1000

SUMMARY

A numerical method will be presented to solve the three-dimensional Navier–Stokes equations in combination with a full Reynolds-stress turbulence model. Computations will be shown for three complex flowfields. The results of the Reynolds-stress model will be compared with those predicted by two different versions of the $k-\omega$ model. It will be shown that an improved version of the $k-\omega$ model gives as accurate results as the Reynolds-stress model.

INTRODUCTION

Faster computer performance and improved numerical methods not only allow the numerical computation of more complex flowfields, but also enable the use of higher order turbulence models in Reynolds averaged Navier–Stokes computations. This is reflected by an increasing number of industrial applications utilizing one-equation or two-equation models instead of the much cheaper algebraic models. These improvements allow the research community to go one step further and to adopt full second-order closure models (full Reynolds-stress models) for the computation of complex three-dimensional flowfields.

The first part of the paper deals with the implementation of a Reynolds-stress model (RSM) into a Navier–Stokes code. The Navier–Stokes method is the INS3D code developed by S. E. Rogers and D. Kwak (ref. 1). It solves the Reynolds-averaged incompressible Navier–Stokes equations in general curvilinear coordinates with a pseudo-compressibility method. The RSM used in this study is the multiscale (MS) model of D. C. Wilcox (ref. 2). In this model the Reynolds-stresses are partitioned into two sets of scales. The large eddies, which act inviscidly, and the small eddies that are isotropic and provide the dissipation. The main advantage of this partitioning is that no diffusion terms appear in the equations for the large eddies, at the expense that one more equation has to be solved, compared to a single scale RSM. It should be noted that the most important part of the model, the pressure-strain term, is identical to the Launder-Reece and Rodi model (ref. 3).

The implementation of an RSM into a Navier–Stokes code is not a trivial matter and can lead to severe stability problems (refs. 4 and 5). The discretization and the linearization of the equations is of crucial importance to the success of the computations. In the present approach, the equations are discretized with a higher order upwind scheme. In order to enhance stability, a total variation diminishing (TVD) (ref. 6) limiter is imposed on the numerical fluxes. Furthermore, the eddy-viscosity formulation of the underlying two-equation model is retained in the implicit side of the mean flow equations to enhance diagonal dominance. This approach is similar to that of an apparent eddy-viscosity adopted in reference 4, except that the apparent viscosity is isentropic in the present discretization.

In the second part of the paper, results will be shown for four increasingly complex flowfields. The first flow is a zero pressure gradient flat plate boundary layer, which is mainly included as a consistency check for the numerical implementation. The second problem is an adverse pressure gradient flow with separation (refs. 7 and 8). The third is a flow over a circular cylinder, with a rotating and a stationary section (refs. 8 and 9) and the last is a fully three-dimensional pressure-driven boundary layer flow (ref. 10). All flowfields have also been computed with the $k-\omega$ two equation model in its original form and in a modified version recently proposed by the author for adverse pressure gradient flows (ref. 11).

Each of the flowfields focuses on a different aspect of the potential superiority of the RSM over the two-equation models. In the adverse pressure gradient flow, the main difference between the $k-\omega$ model and the RSM is that the latter accounts properly for the transport of the Reynolds stresses. The spinning cylinder flow will investigate the potential of the RSM to predict strong curvature effects that are known to be beyond the scope of eddy-viscosity models. The three-dimensional pressure-driven boundary layer flow will show whether the RSM is able to properly predict the differences between the stress and the strain direction as well as the reduction of the turbulent shear-stress observed experimentally in three-dimensional flows (refs. 9 and 12).

EQUATIONS

In the following section all relevant equations (ref. 2) will be given. For the sake of clarity the equations are written for a cartesian coordinate system, although the computations are performed with the equations transformed into general curvilinear coordinates.

Mass conservation:

$$\frac{\partial u_i}{\partial x_i} = 0 \tag{1}$$

Momentum conservation:

$$\frac{\partial \rho u_i}{\partial t} + \frac{\partial \rho u_j u_i}{\partial x_j} = -\frac{\partial p}{\partial x_i} + \frac{\partial \hat{\tau}_{ij}}{\partial x_j} \tag{2}$$

Turbulent kinetic energy:

$$\frac{\partial \rho k}{\partial t} + \frac{\partial \rho u_j k}{\partial x_j} = \tau_{ij}\frac{\partial u_i}{\partial x_j} - \beta^* \rho \omega k + \frac{\partial}{\partial x_j}\left[(\mu + \sigma^* \mu_t)\frac{\partial k}{\partial x_j}\right] \tag{3}$$

Specific dissipation equation:

$$\frac{\partial \rho \omega}{\partial t} + \frac{\partial \rho u_j \omega}{\partial x_j} = \frac{\gamma \omega}{k}\tau_{ij}\frac{\partial u_i}{\partial x_j} - \beta \rho \omega^2 - \xi \beta \rho \omega \sqrt{\Omega_{mn}\Omega_{mn}} + \frac{\partial}{\partial x_j}\left[(\mu + \sigma \mu_t)\frac{\partial \omega}{\partial x_j}\right] \tag{4}$$

Upper partition stress tensor:

$$\frac{\partial \rho T_{ij}}{\partial t} + \frac{\partial \rho u_k T_{ij}}{\partial x_k} = -P_{ij} + E_{ij} \tag{5}$$

In the above notation, u_i is the velocity vector, x_i carthesian coordinates, k the turbulent kinetic energy, ω the specific dissipation rate, ρ the density, t the time, p the pressure, $\hat{\tau}_{ij}$ the sum of the molecular and the Reynolds-stress tensor, T_{ij} the upper partition stress tensor and τ_{ij} the Reynolds-stress tensor. The eddy viscosity $\nu_t = \mu_t/\rho$ is defined as follows:

$$\nu_t = \frac{k}{\omega} \tag{6}$$

The mean strain rate S_{ij} and the mean rotation tensor Ω_{ij} are

$$S_{ij} = \frac{1}{2}\left(\frac{\partial u_i}{\partial x_j} + \frac{\partial u_j}{\partial x_i}\right) \tag{7}$$

$$\Omega_{ij} = \frac{1}{2}\left(\frac{\partial u_i}{\partial x_j} - \frac{\partial u_j}{\partial x_i}\right) \tag{8}$$

The Reynolds-stress tensor is computed from the upper partition stress tensorT_{ij}:

$$\tau_{ij} = \rho T_{ij} - \frac{2}{3}\rho e \delta_{ij} \tag{9}$$

where e is the energy of the eddies in the lower partition. The value of e can be computed by contracting equation (9) (note that T_{ii} is negative):

$$e = k + \frac{1}{2}T_{ii} \tag{10}$$

The tensor E_{ij} defines the transfer from the upper to the lower partition energies:

$$E_{ij} = -c_1\beta^*\omega\left(\tau_{ij} + \frac{2}{3}\rho k\delta_{ij}\right) + \hat{\alpha}P_{ij} + \hat{\beta}D_{ij} + \hat{\gamma}\rho k S_{ij} + \frac{2}{3}\rho\omega k\left(1 - \frac{e}{k}\right)^{\frac{2}{3}}\delta_{ij} \tag{11}$$

The tensors P_{ij} and D_ij are production tensors defined by

$$P_{ij} = \tau_{im}\frac{\partial u_j}{\partial x_m} + \tau_{jm}\frac{\partial u_i}{\partial x_m} \tag{12a}$$

$$D_{ij} = \tau_{im}\frac{\partial u_m}{\partial x_j} + \tau_{jm}\frac{\partial u_m}{\partial x_i} \tag{12b}$$

The model constants are

$\hat{\alpha} = 42/55$	$\hat{\beta} = 6/55$	$\hat{\gamma} = 1/4$
$\beta = 3/40$	$\gamma = \left(1 + \xi\sqrt{\beta^*}\right)\beta/\beta^* - \sigma\kappa^2/\sqrt{\beta^*}$	$\sigma = 1/2$
$\beta^* = 9/100$	$\xi = 1$	$\sigma^* = 1/2$

$$C_1 = 1 + 4(1 - e/k)^{(3/2)} \tag{13}$$

In case the computations are performed with the two-equation $k-\omega$ model, the value of ξ is $\xi = 0$ (ref. 15). The Reynolds-stress tensor is then defined as

$$\tau_{ij} = 2\mu_t S_{ij} - \frac{2}{3}k\delta_{ij} \tag{14}$$

The author (ref. 11) has recently proposed a modification to the two-equation $k-\omega$ model that accounts more realistically for the transport of the principal shear-stress component than equation (6). In the modified model the eddy-viscosity is defined by

$$\nu_t = min\left(\frac{k}{\omega}, \frac{a_1 k}{Q}\right) \tag{15}$$

where Q is the absolute value of the vorticity and $a_1 = 0.3$. The rationale behind this modification is that the equation for the principal shear-stress $\left(\overline{-u'v'}\right)$ in a boundary layer ($Q = \frac{\partial u}{\partial y}$) can be rewritten as follows:

$$\left(\overline{-u'v'}\right) = \frac{k}{\omega}Q = \sqrt{\frac{Production_k}{Dissipation_k}}a_1 k \tag{16}$$

In case of an adverse pressure gradient flow the ratio of production to dissipation can be significantly larger than one in the outer part of the boundary layer, making the shear-stress larger than $a_1 k$, contrary to experimental evidence. Equation (15) ensures that $\left(\overline{-u'v'}\right) \leq a_1 k$. This approach is very similar to the one taken in the Johnson-King model (ref. 13). There a baseline model is supplemented by a transport equation for the principal shear-stress that is based on the assumption that $\overline{-u'v'} = a_1 k$ in the outer part of the boundary layer. In case of the $k-\omega$ model this assumption can be satisfied by applying equation (15).

For the two-equation models the specific dissipation ω is computed from

$$\frac{\partial \rho\omega}{\partial t} + \frac{\partial \rho u_j \omega}{\partial x_j} = \gamma 2 S_{ij} \frac{\partial u_i}{\partial x_j} - \beta \rho \omega^2 + \frac{\partial}{\partial x_j}\left[(\mu + \sigma\mu_t)\frac{\partial \omega}{\partial x_j}\right] \tag{17}$$

If the modified version of the $k-\omega$ model is used, the diffusion constants were changed to

$$\sigma^* = 0.85, \quad \sigma = 0.6$$

The two constants have been optimized to obtain good results for a zero pressure gradient flat plate boundary layer.

NUMERICAL METHOD

The mean flow equations are solved by the INS3D code of S. E. Rogers and D. Kwak (ref. 1) which is based on a pseudo-compressibility method. The convective terms are upwind differenced with a third-order flux-difference approach. The viscous fluxes are differenced with second-order accurate central differences. The linear equations resulting from the first-order backward Euler time differencing are solved with an implicit line relaxation scheme. The same methodology used in INS3D has been applied to the solution of the turbulence equations. The turbulence equations are solved decoupled from the mean flow equations. This means that the turbulence quantities are kept constant during one integration step of the mean flow and vice versa. Furthermore, the turbulence equations are solved decoupled from one another as scalar equations. This approach is justified by the fact that they are coupled mainly through the production and dissipation terms, unlike the much stronger coupling of the mean flow equations through the convection and the pressure terms. The advantage of the scalar treatment is that it is much easier and faster to invert eight tridiagonal matrices than one 8×8 block tridiagonal matrix.

The main difference in the numerical procedure for the mean flow and the turbulence equations is that a total variation diminishing (TVD) scheme is applied to the latter. TVD schemes have been developed to prevent oscillations of the mean flow quantities near shock waves in compressible flows. Since there are no shock waves in the present incompressible applications, it is not necessary to apply a TVD scheme to the mean flow equations. However, the turbulence equations can have weak solutions (discontinuity in the derivative) (ref. 14) near the boundary layer edge. A higher order upwind scheme can lead to small oscillations in this region. Note that the turbulence quantities approach small values at the boundary layer edge and that the oscillations can bring them close to zero. This in turn can cause spikes in the ratios of turbulence quantities that appear in the production and dissipation terms. The TVD scheme has not only proven helpful in connection with the RSM, but also with the two-equation

models, where small undershoots in ω can lead to overshoots in ν_t. Similar effects have been seen with $k-\epsilon$ models.

In the following, ϕ stands for any of the turbulence quantities of equations (3), (4), and (5) and P and D are the corresponding production and destruction terms (divided by J) in that equation. Transformation of the equations into a curvilinear coordinate system $\xi_i, i = 1,3$ and application of the summation convention gives

$$\frac{\partial}{\partial t}\left(\frac{\phi}{J}\right) + \frac{\partial}{\partial \xi_l}\left(\frac{1}{J}\frac{\partial \xi_l}{\partial x_i}u_i\phi\right) = P - D + \frac{\partial}{\partial \xi_l}\left(\frac{1}{J}\frac{\partial \xi_l}{\partial x_i}\frac{\partial \xi_k}{\partial x_i}\tilde{\nu}\frac{\partial \phi}{\partial \xi_k}\right) \tag{18}$$

or in short notation:

$$\frac{\partial}{\partial t}\left(\frac{\phi}{J}\right) + \frac{\partial}{\partial \xi_l}\left(f_l\right) = P - D + \frac{\partial}{\partial \xi_l}\left(f_l^*\right) \tag{19}$$

where J is the Jacobian of the coordinate transformation. The effective viscosity $\tilde{\nu}$ is equal to $\tilde{\nu} = \nu + \sigma^*\nu_t$ for the k-equation, $\tilde{\nu} = \nu + \sigma\nu_t$ for the ω equation and $\tilde{\nu} = 0$ for the equations of the upper partition stress tensor.

Spatial Discretization

The difference scheme for the convection terms is given for the flux f in the ξ direction:

$$\frac{\partial f}{\partial \xi} \approx \frac{\hat{f}_{j+\frac{1}{2}} - \hat{f}_{j-\frac{1}{2}}}{\Delta\xi} \tag{20}$$

with

$$\hat{f}_{j+\frac{1}{2}} = h_{j+\frac{1}{2}} - \frac{1}{6}\tilde{df}^-_{j+\frac{3}{2}} - \frac{1}{3}\tilde{df}^-_{j+\frac{1}{2}} + \frac{1}{3}\tilde{df}^+_{j+\frac{1}{2}} + \frac{1}{6}\tilde{df}^+_{j-\frac{1}{2}} \tag{21}$$

The first-order flux $h_{j+\frac{1}{2}}$ is defined as follows:

$$h_{j+\frac{1}{2}} = \frac{1}{2}\left[f(\phi_{j+1}) + f(\phi_j)\right] - \frac{1}{2}\left[df^+_{j+\frac{1}{2}} - df^-_{j+\frac{1}{2}}\right] \tag{22}$$

The flux differences are

$$df^{\pm}_{j+\frac{1}{2}} = \lambda^{\pm}_{j+\frac{1}{2}}\left(\phi_{j+1} - \phi_j\right) \tag{23}$$

where the positive and the negative parts of the eigenvalues in ξ are

$$\lambda^{\pm}_{j+\frac{1}{2}} = \frac{1}{2}\left(\lambda \pm |\lambda|\right) \tag{24a}$$

$$\lambda = \frac{1}{J}\frac{\partial \xi}{\partial x_i}u_i \tag{24b}$$

The flux limited values of the TVD scheme df are defined by the minmod function given in (ref. 6):

$$\tilde{df}^{-}_{j+\frac{3}{2}} = minmod\left[df^{-}_{j+\frac{3}{2}}, \chi df^{-}_{j+\frac{1}{2}}\right] \tag{25a}$$

$$\tilde{\tilde{df}}^{-}_{j+\frac{1}{2}} = minmod\left[df^{-}_{j+\frac{1}{2}}, \chi df^{-}_{j+\frac{3}{2}}\right] \tag{25b}$$

$$\tilde{df}^{+}_{j+\frac{1}{2}} = minmod\left[df^{+}_{j+\frac{1}{2}}, \chi df^{+}_{j-\frac{1}{2}}\right] \tag{25c}$$

$$\tilde{\tilde{df}}^{+}_{j-\frac{1}{2}} = minmod\left[df^{+}_{j-\frac{1}{2}}, \chi df^{+}_{j+\frac{1}{2}}\right] \tag{25d}$$

A value of $\chi = 3$ was used for the parameter of the TVD scheme. The minmod function is defined as follows:

$$minmod[x, y] = sign(x) max\left[0, min[|x|, y sign(x)]\right] \tag{26}$$

Note that the limited fluxes in equation (25d) are identical to their unlimited values over most of the computational domain, and that the limiter is activated only if the fluxes at neighboring points have different signs, or are different by a factor of χ. The unlimited scheme is third-order accurate for the convection terms.

The viscous terms f^* in equation (19) are discretized with standard second-ordercentral differences and the production and dissipation terms are simply transformed by applying the chain rule.

Time Discretization

The implicit time discretization of the equations is the same as used in INS3D (ref. 1) for the mean flow equations:

$$\left[\frac{1}{J\Delta\tau} I + \left(\frac{\partial \tilde{R}}{\partial \phi}\right)^{n}\right]\left(\phi^{n+1} - \phi^{n}\right) = -R^{n} \tag{27}$$

where n denotes the time level and R the residual of the discretized equations. $\frac{\partial \tilde{R}}{\partial \phi}$ is an approximate Jacobian of the residual R, which accounts only for the first-order terms in the upwind differencing ($h_{j\pm\frac{1}{2}}$ in eq. (21)) and the orthogonal terms of the viscous expressions. Forming the exact Jacobian is too costly and destroys the tridiagonal structure of the matrices. One of the crucial points in the discretization of higher order turbulence models is the linearization of the source terms. Relatively good convergence properties have been achieved with the following approximate linearizations:

$$\frac{\partial\left(P_k - D_k\right)}{\partial k} \approx -\frac{(D_k)}{k} \tag{28a}$$

$$\frac{\partial\left(P_\omega - D_\omega\right)}{\partial \omega} \approx -2\beta\omega\frac{1}{J} \tag{28b}$$

$$\frac{\partial\left(-P_{ij} + E_{ij}\right)}{\partial T_{ij}} \approx -C_{1max}\beta^{*}\omega\frac{1}{J} \tag{28c}$$

It was found to be advantageous to use the largest possible value $C_{1max} = 5$ for C_1 in equation (13) in the implicit part to enhance diagonal dominance. Note that all the approximations to the implicit part of the equations have no effect on the steady-state solution.

The linear equation system resulting from equation (27) has the following form (ref. 1):

$$\underline{\underline{M}}\Delta\underline{\phi} = \underline{R} \tag{29}$$

where $\underline{\underline{M}}$ is, after appropriate numbering of the equations, a banded matrix of the general form:

$$\underline{\underline{M}}\left(m_{j,k,l-1}, 0, .., m_{j,k-1,l}, 0, .., m_{j-1,k,l}, m_{j,k,l}, m_{j+1,k,l}, 0, .., m_{j,k+1,l}, 0, .., m_{j,k,l+1}\right) \tag{30}$$

Equation (29) is solved by a Gauss-Seidel line relaxation method:

$$\begin{aligned}\tilde{\underline{\underline{M}}}\left(m_{j-1,k,l}, m_{j,k,l}, m_{j+1,k,l}\right)\Delta\phi^{\overline{m}+1} = \underline{R}^n - m_{j,k,l-1}\Delta\phi^{\overline{m}}_{j,k,l-1} - m_{j,k-1,l}\Delta\phi^{\overline{m}}_{j,k-1,l} \\ -m_{j,k+1,l}\Delta\phi^{\overline{m}}_{j,k+1,l} - m_{j,k,l+1}\Delta\phi^{\overline{m}}_{j,k,l+1}\end{aligned} \tag{31}$$

where $\overline{m}$ is the iteration level. The tridiagonal system of equation (31) is solved with a LU decomposition method. In order to enhance the stability of the solution procedure, the eddy-viscosity formulation is maintained in the implicit part of the mean flow equations.

Boundary Conditions

All boundary conditions are treated implicitly to preserve the stability properties of the implicit scheme. At a no-slip condition, the mean flow velocities are set to zero as well as the pressure gradient normal to the wall. All turbulent quantities, except ω are also set to zero. As pointed out by Wilcox (ref. 15), ω satisfies the following equation near the wall:

$$\omega \rightarrow \frac{6\nu}{\beta y^2} \qquad \text{as} \qquad y \rightarrow 0 \tag{32}$$

Wilcox recommends to specify this analytical solution for the first few gridpoints away from the wall explicitly. The present author found it much easier and as accurate to implement the following boundary condition:

$$\omega = 10\frac{6\nu}{\beta(\Delta y)^2} \qquad \text{at} \qquad y = 0 \tag{33}$$

where Δy is the distance to the next point away from the wall. Equation (33) simulates the boundary condition (eq. (32)) without the need of changing the solution at interior points. It should be noted that models based on the ω-equation give accurate results if the near wall values of ω are sufficiently large. Both equations (32) and (33) satisfy this demand. The results are not sensitive to the factor (10) used in equation (33).

At a slip surface, the normal pressure gradient is again zero and so is the velocity normal to the surface. Furthermore, the gradients normal to the surface of the two velocity components lying in the plane of the surface are also set to zero.

At an inflow and outflow boundary, the mean flow quantities are determined by the method of characteristics. This means that for an inflow condition the velocity components are specified and the pressure is determined from within the domain, whereas for an outflow condition the pressure is given and the velocities are determined by the characteristic relations. The turbulence quantities are specified at inflow boundaries; at outflow boundaries, a zero gradient is assumed.

Two of the computed flowfields have a rotational symmetry. In these cases, the gradients of all quantities in the circumferential direction are set to zero.

RESULTS

Flat Plate Boundary Layer

The first set of computations has been performed for a flat plate zeropressure gradient boundary layer. The number of gridpoints was $60 \times 3 \times 80$. Although the flow is two-dimensional, it is necessary to introduce three planes in the lateral direction since the code solves only three-dimensional flow problems. Resolution studies with a $40 \times 3 \times 80$ and a $90 \times 3 \times 90$ grid show that the solutions are grid independent. All grid refinement studies have been done with the $k - \omega$ model for economic reasons, but are believed to be valid also for the multiscale model because of the strong similarities between the equations. Figure 1 shows the results of the computations. Obviously, all models give very similar results, both in the c_f-distribution and in the law-of-the-wall plot. It should be mentioned at this point, that the results computed with the $k - \omega$ model have a strong dependence on the freestream values of ω, as shown in reference 16. In order to ensure unambigious solutions, the proper inflow values for ω given in reference 16 have been specified. It should be noted that the freestream dependency of the model is not removed by the modifications to the eddy-viscosity given in equation (15).

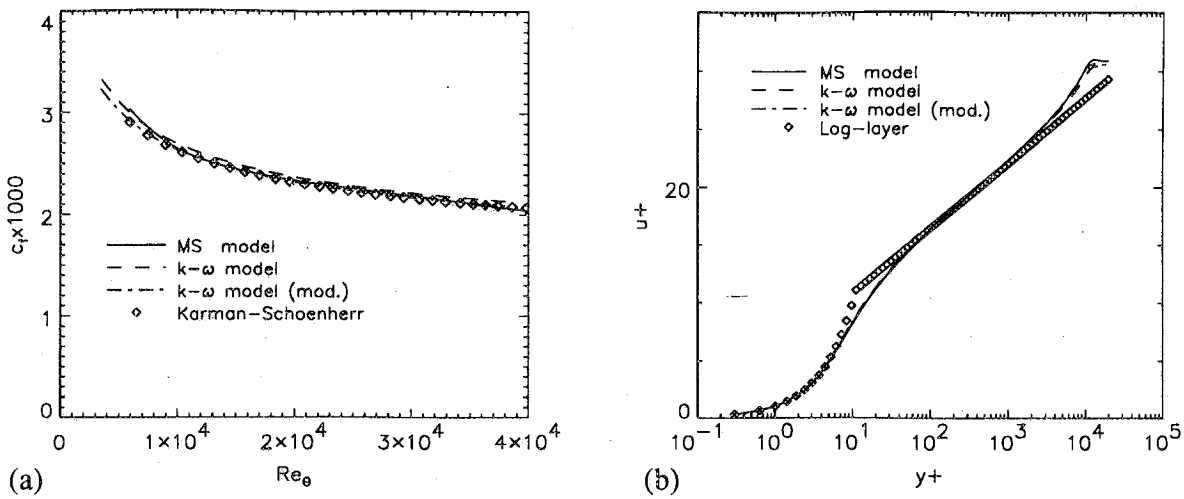

Figure 1. Flat plate boundary layer. (a) Skin friction, (b) law-of-the-wall.

Adverse Pressure Gradient Flow

The second test case is an adverse pressure gradient boundary layer, developing in the axial direction of a circular cylinder, as reported by D. Driver (refs. 7 and 8). The pressure gradient is strong enough to cause the boundary layer to separate. The computations have been carried out with a $60 \times 3 \times 60$ grid. The grid independence was ensured by a $100 \times 3 \times 100$ gridpoint computation with the $k-\omega$ model.

This flowfield has been computed before by the present author (ref. 11) with a number of different eddy-viscosity models. The best results in that comparison have been obtained with the Johnson-King (JK) model (ref. 13). The major difference between the JK model and equilibrium algebraic eddy-viscosity models is the inclusion of the transport effect of the principal turbulent shear-stress component. One would expect that the RSM and the modified $k-\omega$ model should be able to improve the results of the baseline $k-\omega$ model, since both of them account properly for this transport effect. Note that the modified $k-\omega$ model is based on the same assumption as the JK model, that the shear-stress is proportional to the kinetic energy in the outer part of the boundary layer.

Figure 2 shows the computed c_p distributions in comparison with the experimental data. It is obvious that both the MS model and the modified $k-\omega$ model give superior results over the baseline $k-\omega$ model. The predictions of the two former models are virtually identical and in excellent agreement with the experimental data. Keeping in mind that the c_p distribution is the single most important quantity in aerodynamic computations, the distribution shown in figure 2 gives some hope that properly designed two-equation models and full RSM can give accurate predictions for these flows. A comparison of computed and measured c_f distributions is shown in figure 3. There are only small differences in the predictions of the $k-\omega$ and the MS models, whereas the modified model predicts the minimum wall-shear-stress more accurately, but overpredicts the downstream extent of the separation zone.

The differences seen in figures 2 and 3 are consistent with the velocity profiles depicted in figure 4. The MS and the modified $k-\omega$ model predict higher displacement thicknesses than the $k-\omega$ model

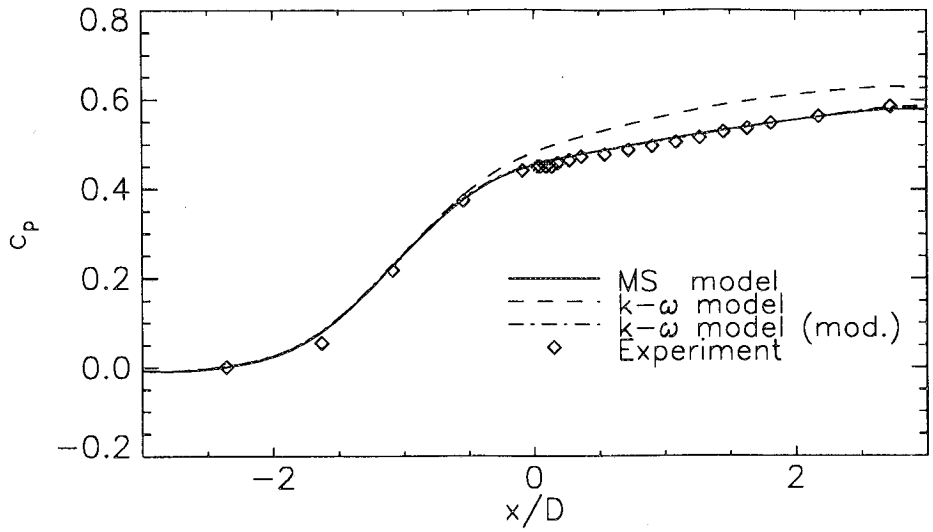

Figure 2. c_p distribution for adverse pressure gradient flow CS0.

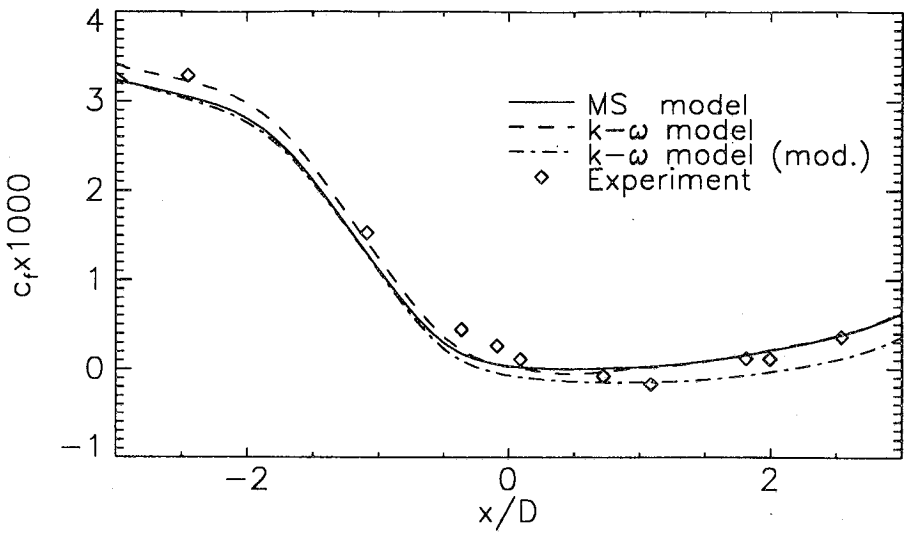

Figure 3. c_f distribution for adverse pressure gradient flow CS0.

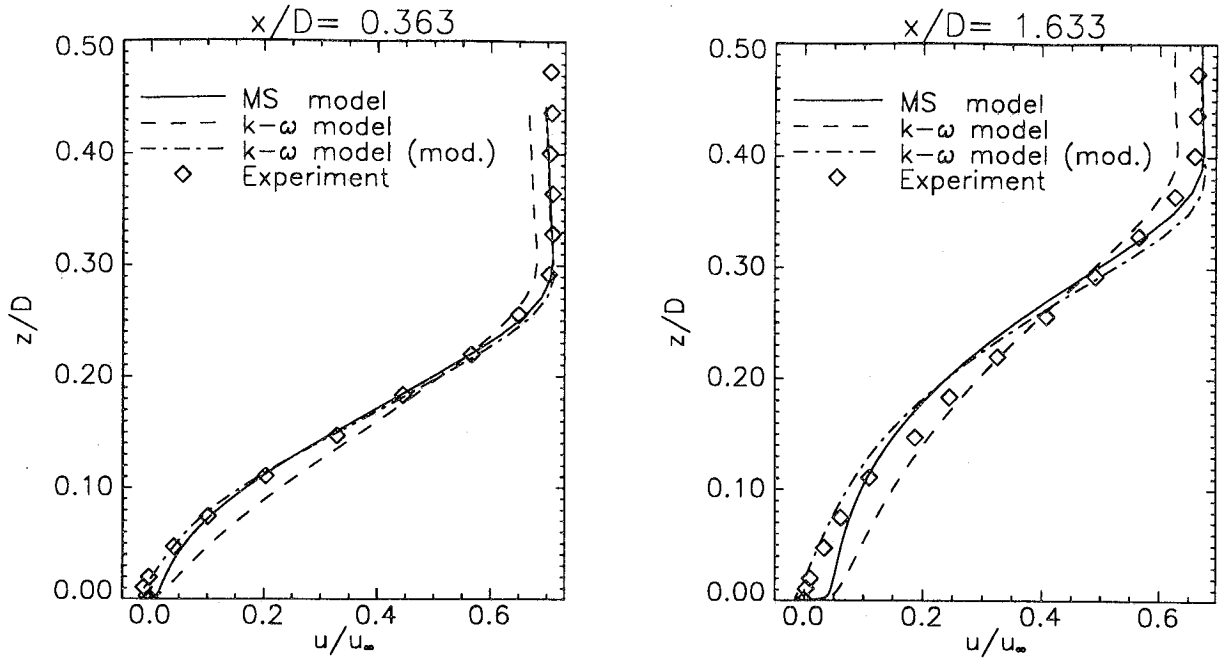

Figure 4. Velocity profiles for adverse pressure gradient flow CS0.

and therefore a superior pressure distribution. Near the wall the modified model is in better agreement with the experimental shape of the profiles and therefore gives lower c_f values.

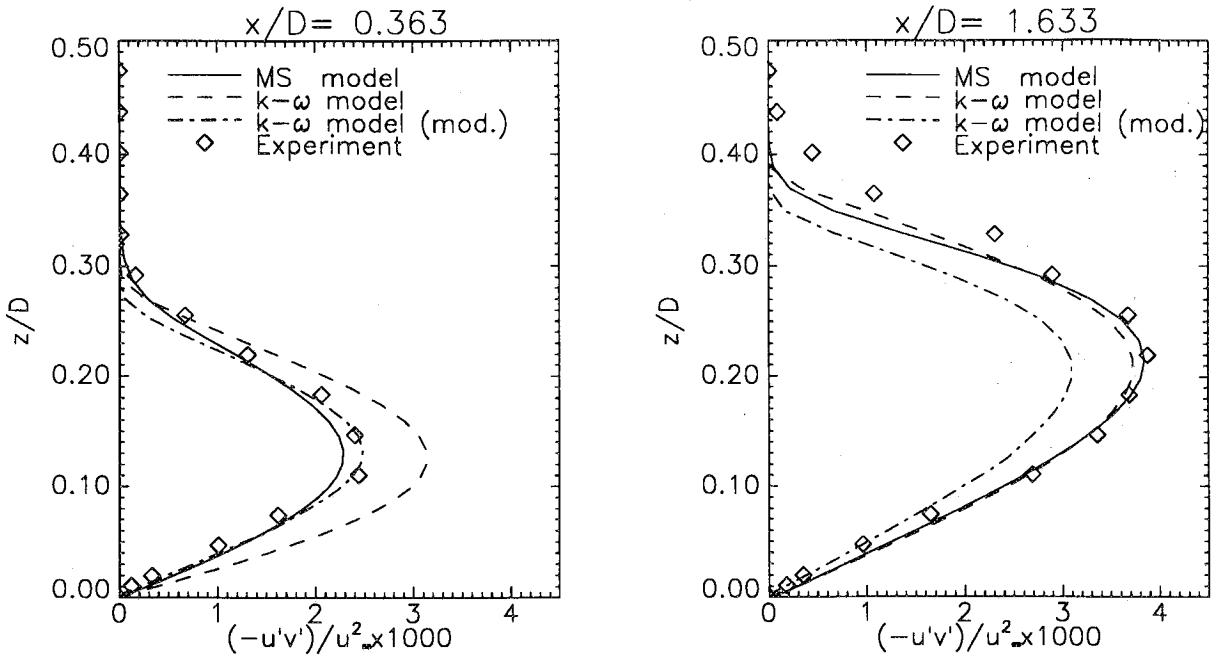

Figure 5. Shear-stress profiles for adverse pressure gradient flow CS0.

The main reasons for the differences in the predictions can be seen in figure 5, showing two turbulent shear-stress profiles at different axial locations. It was found in all computations of this flowfield that the c_p distribution can be predicted accurately if the shear stresses up to separation are computed correctly. Note that the stresses predicted by the MS model and the modified $k-\omega$ model are in close agreement with experiments at $x/D = 0.363$ and that the differences in the predictions at $x/D = 1.633$ are not reflected in the c_p distribution (fig. 3). The reason for the overprediction of the c_p values by the $k-\omega$ model lies in the overprediction of the turbulent shear-stress levels up to separation (fig. 5) and is an immediate consequence of equation (6).

Figure 6 shows the distribution of the normal stresses, as predicted by the MS model. Note that in the present case, $\overline{v'^2}$ is the stress component in circumferential and $\overline{w'^2}$ the one in wall normal direction. The normal stresses are obviously predicted quite well, although slightly too low at $x/D = 0.363$.

The above results confirm the theory motivating the JK model that the main additional complexity in the prediction of adverse pressure gradient flows comes from the importance of the transport terms in the equation for the principal shear-stress. The comparison of the results from the MS and the modified $k-\omega$ model shows that a properly designed two equation model can give as accurate results for this kind of flow as a full Reynolds-stress model.

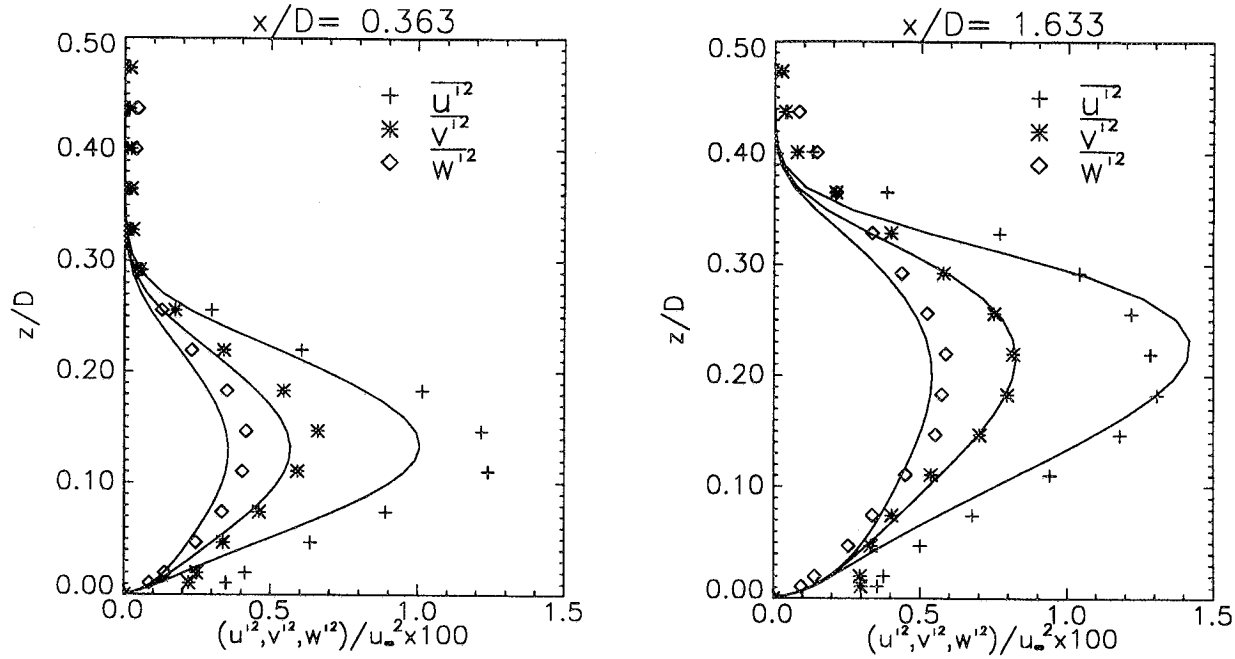

Figure 6. Normal-stress profiles for adverse pressure gradient flow CS0.

Spinning Cylinder Flow

The next problem that was considered is the flow along a circular cylinder with a spinning upstream ($x/D < 0$) and a stationary downstream ($x/D > 0$) section, as reported by D. Driver and J. P. Johnston (refs. 8 and 9). The circumferential surface velocity of the spinning part is equal to the incoming freestream velocity U_∞ in axial direction.

The flow is collateral in the upstream (rotating) part of the cylinder, as noted by Driver et al., which means that the velocity profiles are two-dimensional for an observer moving with the wall. Therefore no three-dimensional effects have to be expected in this region. However, due to strong curvature effects the computation of the upstream flow is by no means trivial. As the flow relaxes back to a purely two-dimensional boundary layer along the stationary part of the cylinder, the three-dimensional, curvature and transport effects are of equal importance, which creates a very challenging problem for all turbulence models.

The computations have been performed on a $90 \times 3 \times 90$ grid. Solutions on a $60 \times 3 \times 60$ grid are only slightly different, confirming the grid independence of the present results.

Figure 7 shows two profiles of the axial velocity at different axial stations. The profile on the left is located on the spinning part of the cylinder and the profile on the right in the three-dimensional interaction region on the stationary part. Figure 8 depicts the circumferential velocity component at the same two stations. Obviously, the profiles in the spinning part of the cylinder $x < 0$ are not computed accurately by any of the models. The near wall gradients of both the u and the v component at $\frac{x}{D} = -0.091$ are severely underpredicted. The reason for this discrepancy is that the models do not pick up the destabilizing effect of the curvature and therefore underpredict the turbulent shear-stresses,

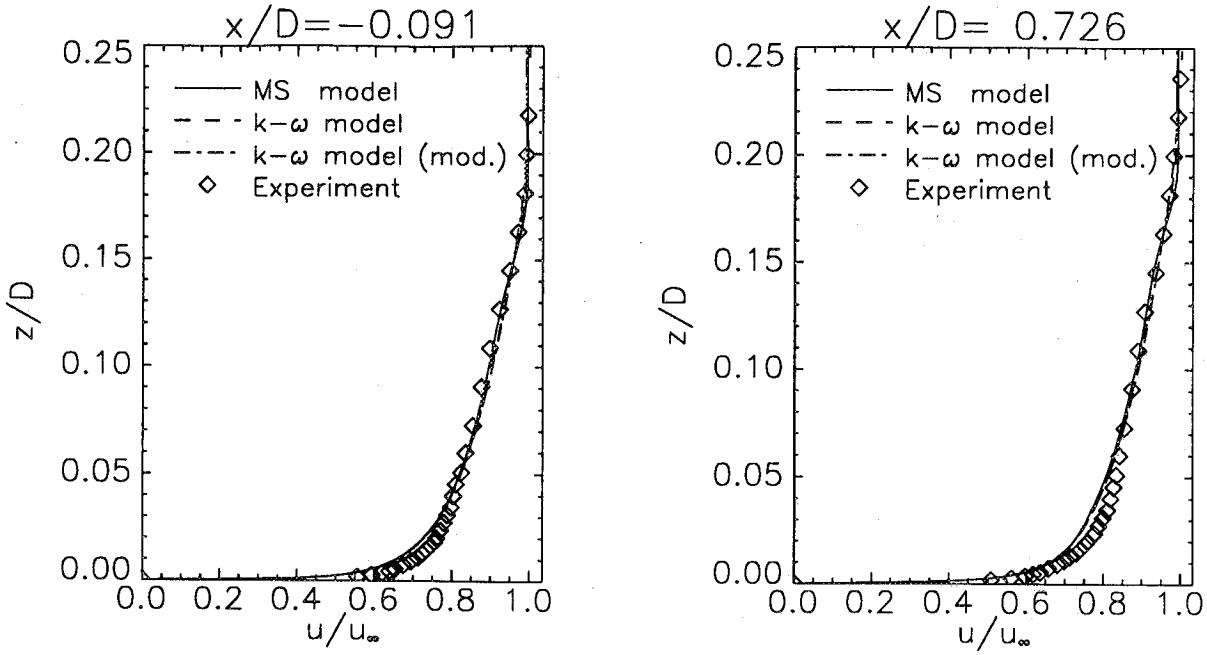

Figure 7. Profiles of axial velocity $\frac{u}{U_\infty}$ for spinning cylinder flow AS1.

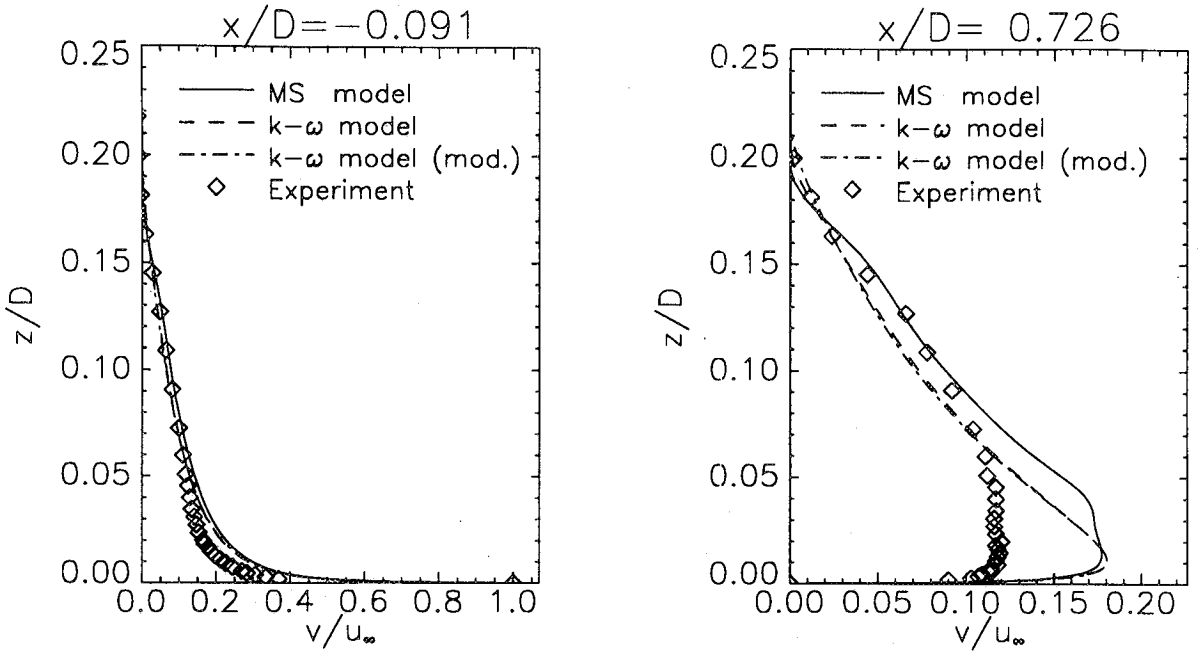

Figure 8. Profiles of circumferential velocity $\frac{v}{U_\infty}$ for spinning cylinder flow AS1.

as seen in figure 9. The MS model gives somewhat higher shear-stress levels than the two-equation models, but failed to meet expectations (refs. 17 and 18) of predicting curvature effects properly.

With regard to the downstream station $\frac{x}{D} = 0.726$, the results of the MS model are also not significantly better than the results of the two-equation models. The shape of the circumferential velocity profile is computed in closer agreement with the experiment (fig. 8), but the absolute values are also significantly higher near the wall. The more realistic shape of the v profile is a result of the improved prediction of the $\overline{v'w'}$ profiles (fig. 9).

Figure 10 shows a comparison of computed and measured turbulent kinetic energy profiles. Note that the results of the MS model and the two-equation models are very close to each other and significantly smaller than the experimental values, again due to the underprediction of the curvature effects. Figure 11 depicts the results of the MS model in more detail by showing the individual normal stresses compared to the experiments.

Figure 12 shows the c_f-distribution along the stationary part of the cylinder. The wall-shear-stress component in axial direction c_{fx} is underpredicted and the component in circumferential direction c_{fy} is overpredicted, which is in agreement with the velocity profiles (fig. 7).

Figure 13 shows a map of the second (II) and third (III) invariant of the anisotropy tensor b_{ij} at two downstream stations. The definitions of the anisotropy tensor and its invariants are

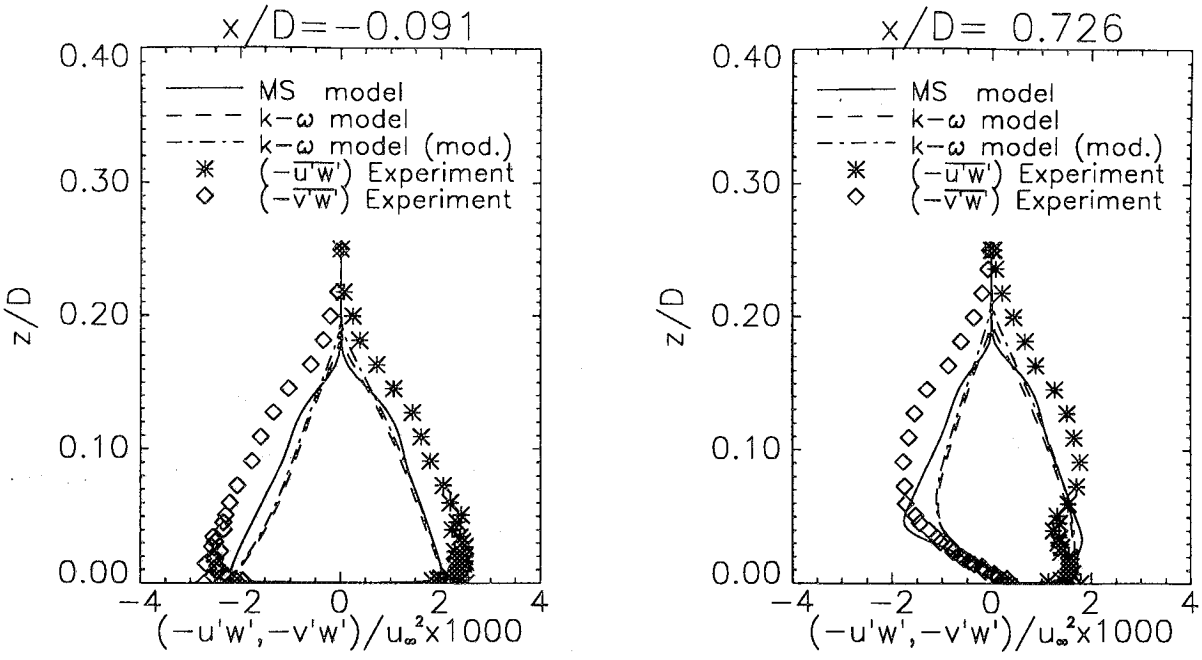

Figure 9. Profiles of axial $(\overline{u'w'})$ and circumferential $(\overline{v'w'})$ shear-stress profiles for spinning cylinder flow AS1.

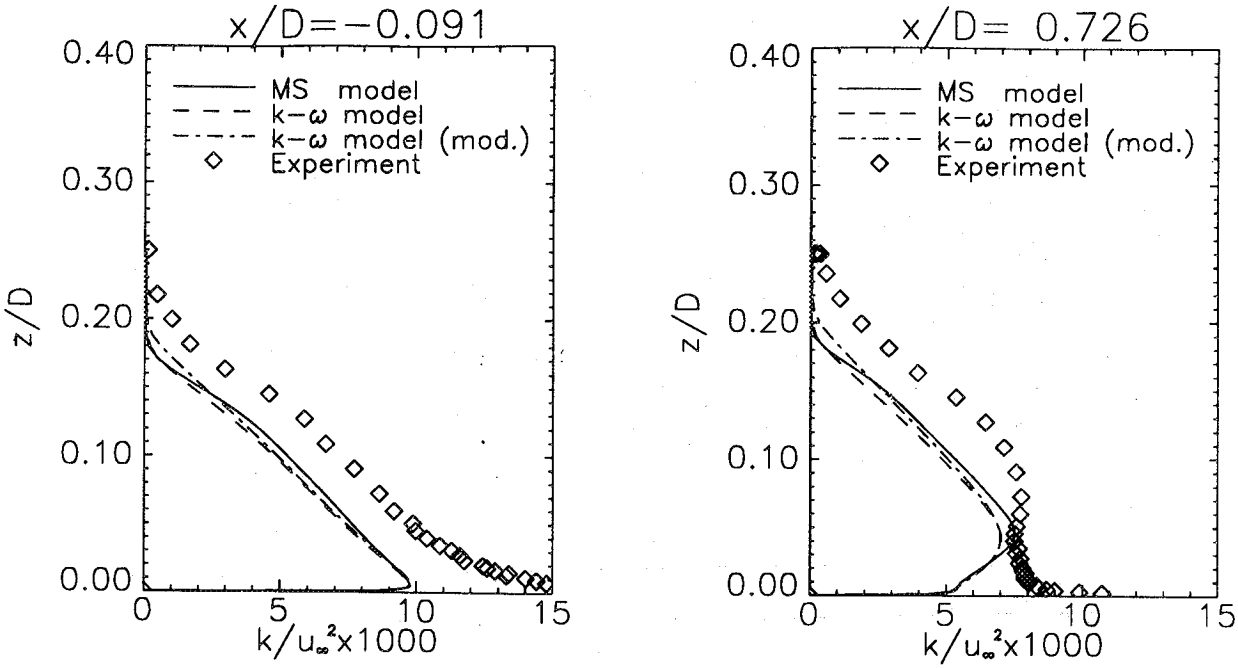

Figure 10. Profiles of turbulent kinetic energy for spinning cylinder flow AS1.

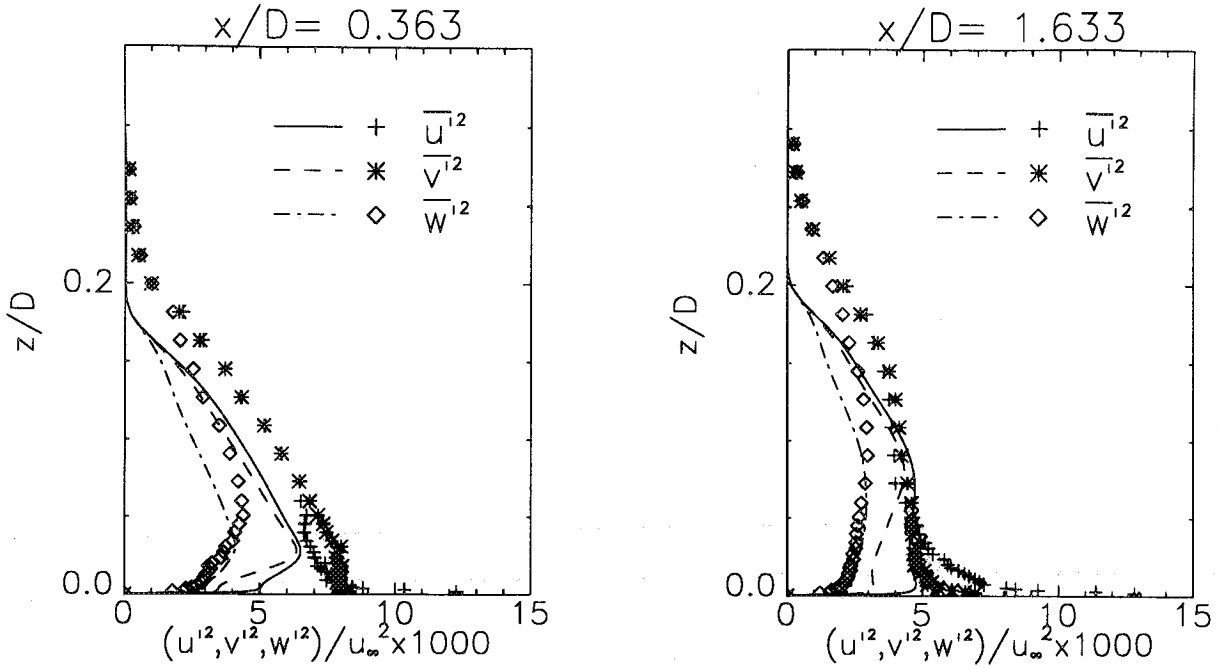

Figure 11. Profiles of normal turbulent stresses, computed from the multiscale model for spinning cylinder flow AS1.

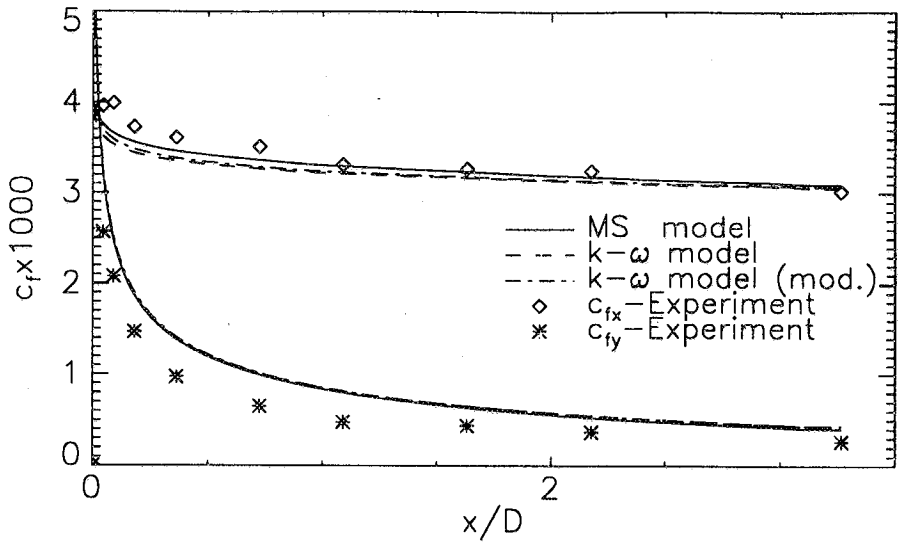

Figure 12. Axial (c_{fx}) and circumferential (c_{fy}) wall-shear-stress distributions for spinning cylinder flow AS1.

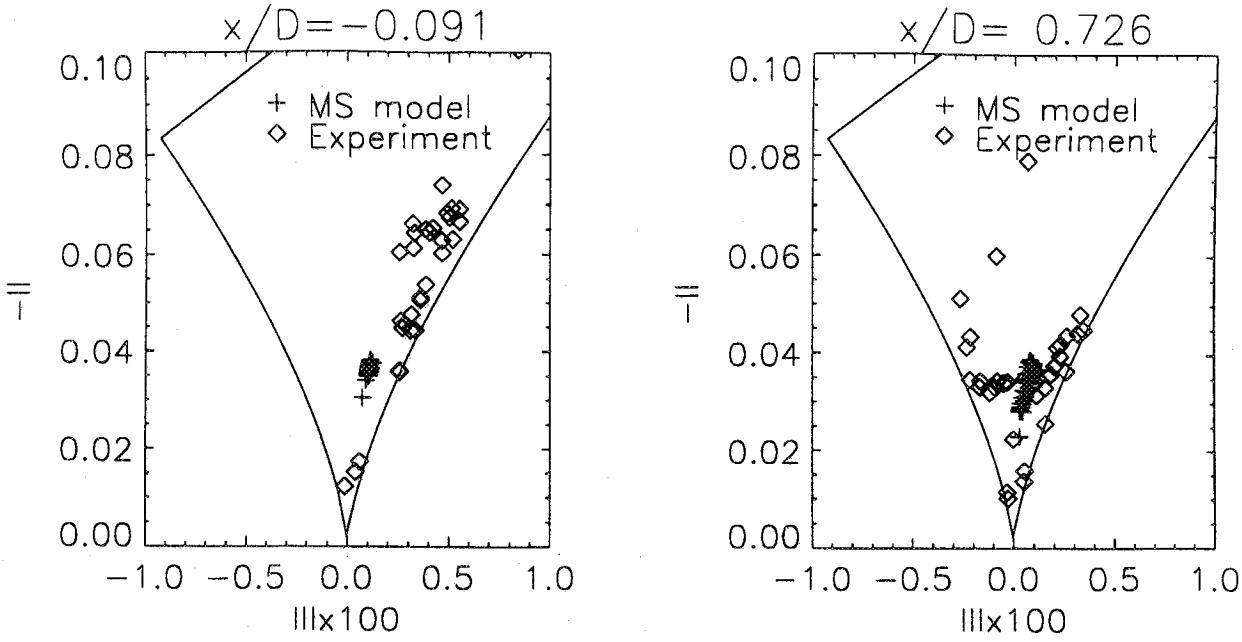

Figure 13. Anisotropy invariant map, computed from the multiscale model for spinning cylinder flow AS1.

$$b_{ij} = \frac{u_i u_j - \frac{2}{3} k \delta_{ij}}{2k} \tag{34}$$

$$II = -b_{ij} b_{ji}/2 \quad , \quad III = b_{ij} b_{jk} b_{ki}/3 \tag{35}$$

The map was introduced by Lumley (ref. 19) to characterize the anisotropy of turbulent flows in a coordinate invariant fashion. Each of the boundaries of the map corresponds to a different asymptotic state of turbulence: the origin is the isotropic state, the upper boundary corresponds to all two-dimensional states, the left boundary represents an axisymmetric contraction and the right boundary an axisymmetric expansion. It is obvious from figure 13 that the predictions of the MS model cover a significantly smaller part of the map than the experimental data. Although the flowfield is highly three-dimensional and has strong curvature effects, the predictions stay very close to their design point for a zero-pressure-gradient flat plate boundary layer. The inability of the model to predict the anisotropic behavior of the flow is suspected to be a shortcoming of the Launder-Reece-Rodi pressure-strain model (ref. 3) underlying the MS model. Results of boundary layer computations, based on the Launder-Reece and Rodi model as reported by Driver (ref. 8), are in very good agreement with the present results, giving further support to this opinion.

Three-Dimensional Pressure Driven Boundary Layer Flow

The flowfield discussed in this section has been investigated experimentally by S. D. Anderson and J. K. Eaton (ref. 10). The experimental setup is shown in figure 14. All dimensions are in centimeters. A two dimensional boundary layer enters the test section and is deflected by a 90° wedge. Due to the strong lateral pressure gradient created by the wedge, highly skewed three-dimensional boundary layer profiles develop downstream. Measurements of the mean velocity and of turbulent correlations are available along the centerline, and along a selected streamline, as shown in figure 14 (experimental ports). In addition to the profile information, lateral static pressure distributions have been measured at seven x-locations outside the boundary layer. In the following, the origin of the coordinate system is located at the tip of the wedge, with the x-coordinate pointing in the direction of the symmetry line (positive x in direction of the incoming flow), the y-coordinate is in the lateral and the z-coordinate in surface normal direction.

The geometry of the test section is symmetric with respect to both the y- and the z-direction, so that in principle, only one quarter of the flowfield needs to be computed. Unfortunately, a small amount of suction was applied in the experiment to the incoming boundary layer on the upper wall, so that the upper and lower incoming boundary layers were slightly different.

Three different sets of computations have been performed with the $k - \omega$ model in order to test the grid dependence and the influence of the asymmetric inflow conditions. First a grid refinement study was performed computing only one quarter of the flowfield. It was found that the computations performed on a $35 \times 35 \times 35$ grid and on a $50 \times 50 \times 50$ grid are in very close agreement with each other. Figure 15 shows a comparison of streamwise and the crossflow mean velocity profiles at the last downstream station of the experiments. Differences further upstream are even smaller. An additional computation was performed on a $40 \times 40 \times 80$ grid, including the upper boundary layer. Results of that computation are also included in figure 15. The inclusion of the upper half of the flowfield obviously

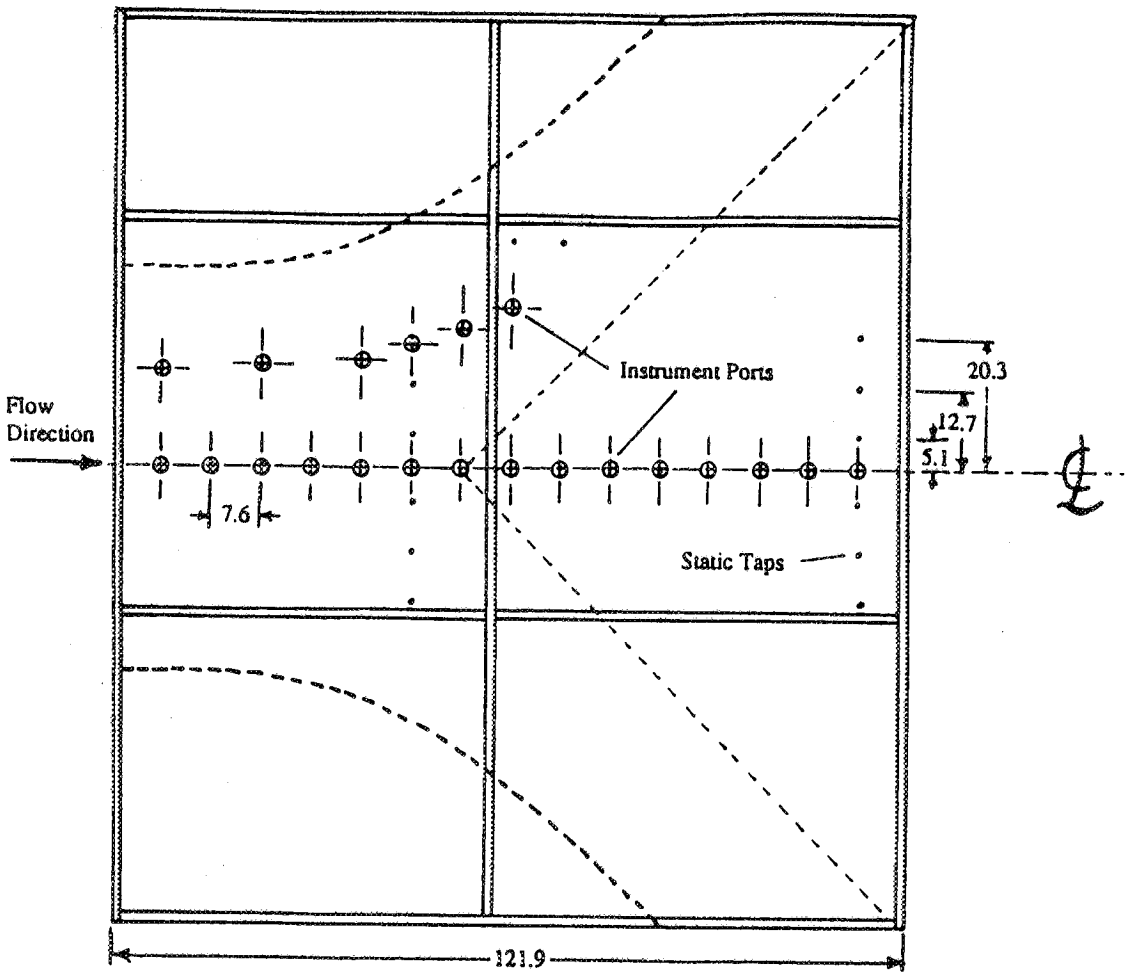

Figure 14. Experimental setup for 90° wedge flow (from ref. 10).

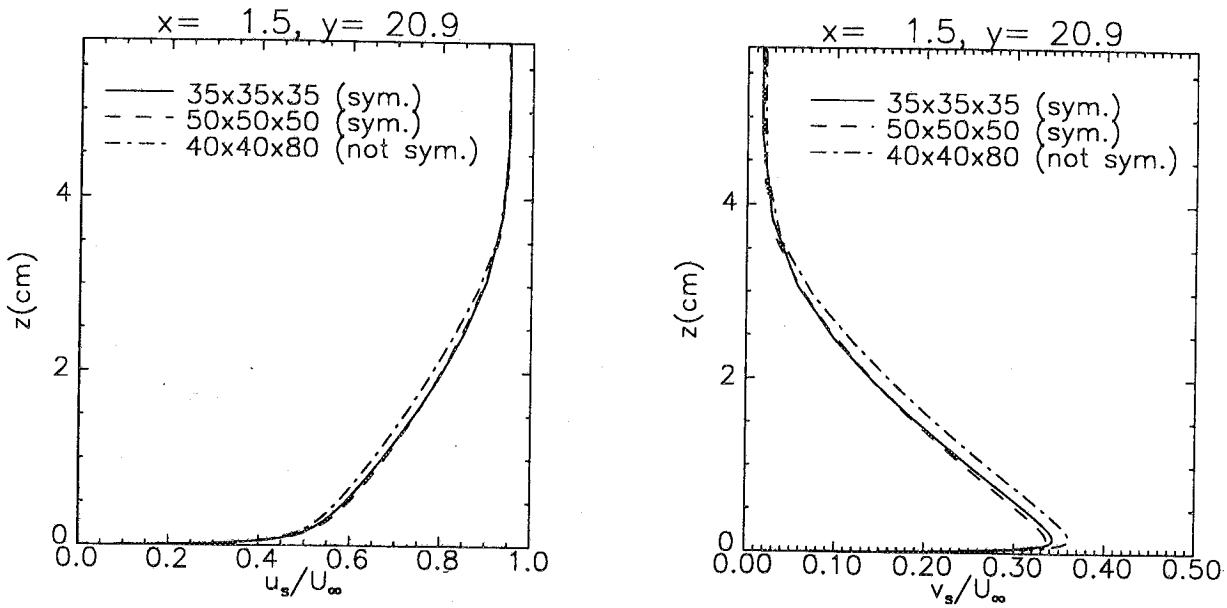

Figure 15. Grid-refinement study for 3D wedge flow.

does not lead to significant changes in the solution. The following results are therefore all for the $50 \times 50 \times 50$ grid with a symmetry condition in the middle of the tunnel.

Figure 16 shows a comparison of computed and experimental pressure distributions for the three different models. Although the differences are not dramatic, the MS- and the modified $k-\omega$ model are in better agreement with the experiments than the original $k-\omega$ model, especially in the downstream region.

Figure 17 shows the velocity profiles along the centerline of the channel. Differences between the models appear only at the station closest to the tip of the wedge. The $k-\omega$ model does not react sufficiently to the adverse pressure gradient and predicts too full a profile shape. The modified $k-\omega$ model is separated at this station, and the MS model is close to separation. Although the MS model is apparently in better agreement with the data, no final conclusion can be drawn from figure 17, because the three hole probe used in the experiments cannot measure separated profiles. Unfortunatelly, no oil-flow pictures are available for this experiment.

A comparison of turbulent shear stress profiles is given in figure 18. Experimental data are only available for the first three stations. The larger symbols at $z = 0$ represent the measured wall-shear stress. The results are very similar to those for the adverse pressure gradient flow cs0 (fig. 5). The

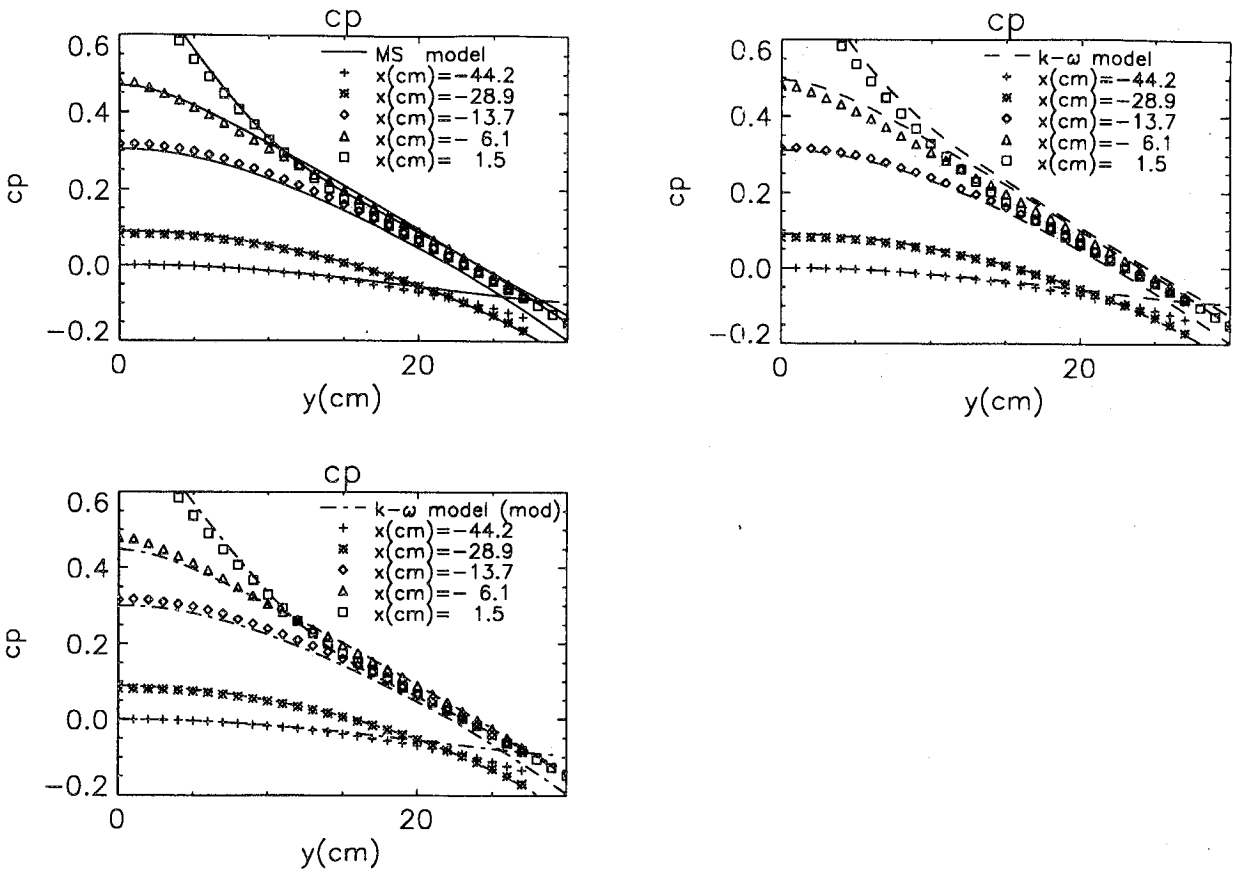

Figure 16. C_p distribution for 3D wedge flow.

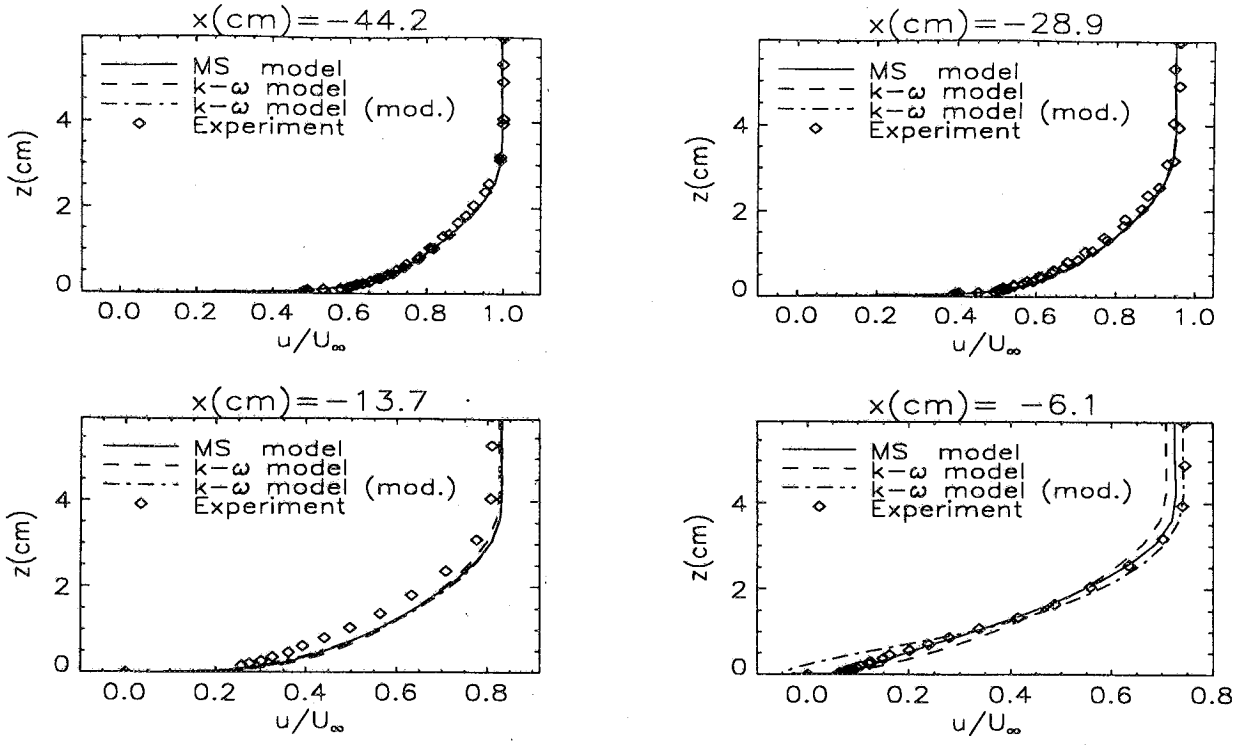

Figure 17. Velocity profiles along centerline for 3D wedge flow.

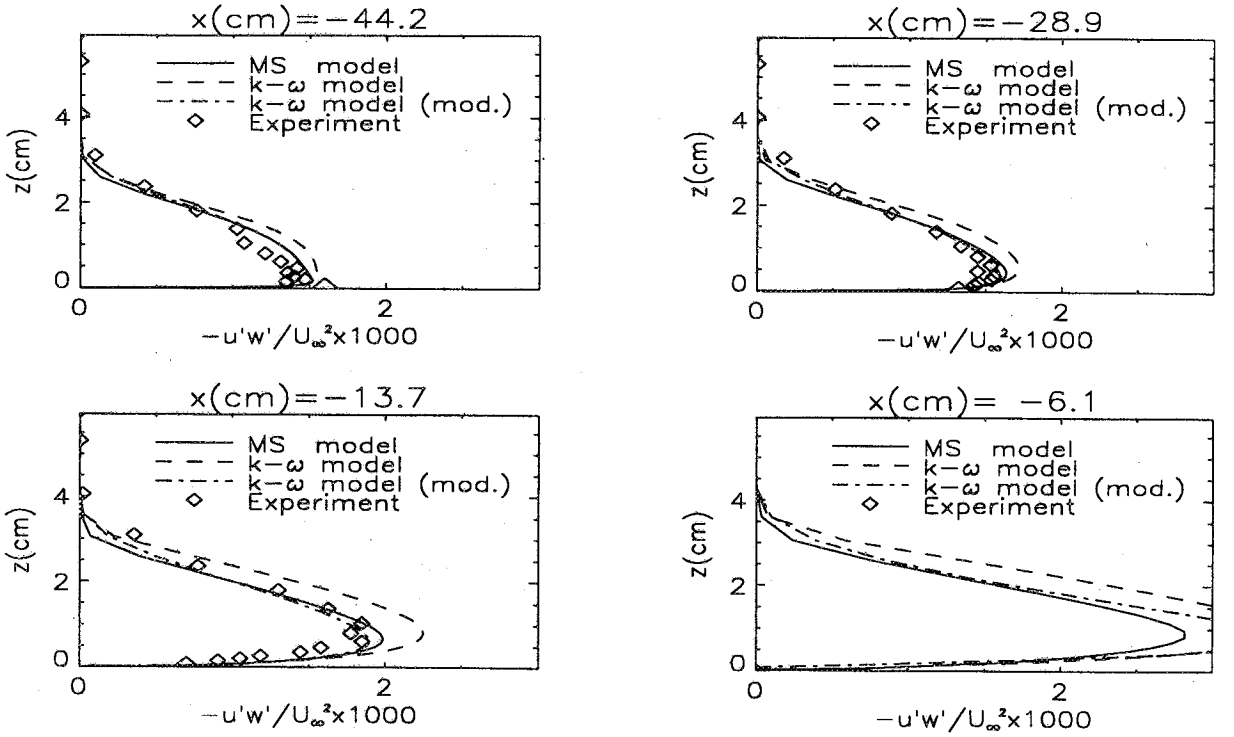

Figure 18. Shear-stress profiles along centerline for 3D wedge flow.

$k-\omega$ model overpredicts the shear stress levels, whereas the other two models are in close agreement with the experiments which in turn leads to more retarded velocity profiles.

The present computation focuses on the performance of the models in the region of three-dimensional boundary layer profiles away from the centerline. Figure 19 shows four streamwise velocity profiles along the selected streamline. The local coordinate system for these plots is aligned with the experimental freestream direction. Figure 20 shows the corresponding crossflow profiles. The modified $k-\omega$ model is obviously closest to the experiments. It predicts the retardation of the streamwise velocity component near the wall, and gives the correct amount of crossflow at the last downstream station. The discrepancies between the computations and the experimental profiles in the upstream portion of the flow might be explained by the failure of all of the models to predict the reduction of the turbulent shear stress shown in figure 21 due to the three-dimensionality of the mean-flow profiles. However, both the MS and the modified $k-\omega$ model predict significantly lower shear-stress values than the original $k-\omega$ model and are therefore closer to the experimental data. Note that experimental stress profiles are only available for the first three stations. The close agreement between the former two models in the prediction of the turbulent shear stresses shows that the advantage of the MS model over the baseline two-equation model is again its ability to account for transport effects. This is also demonstrated by figure 22, showing the shear stresses in the crossflow direction. Again, the MS and the modified two-equation model are in very close agreement with each other and somewhat closer to the experiment. Obviously all models fail to predict the crossflow component of the shear-stress correctly and are therefore not able to predict the correct direction of the shear-stress vector. This has to be expected from the eddy-viscosity models which assume that the stresses are proportional to the strain rate. The MS model in turn solves a separate equation for every stress component and has therefore the

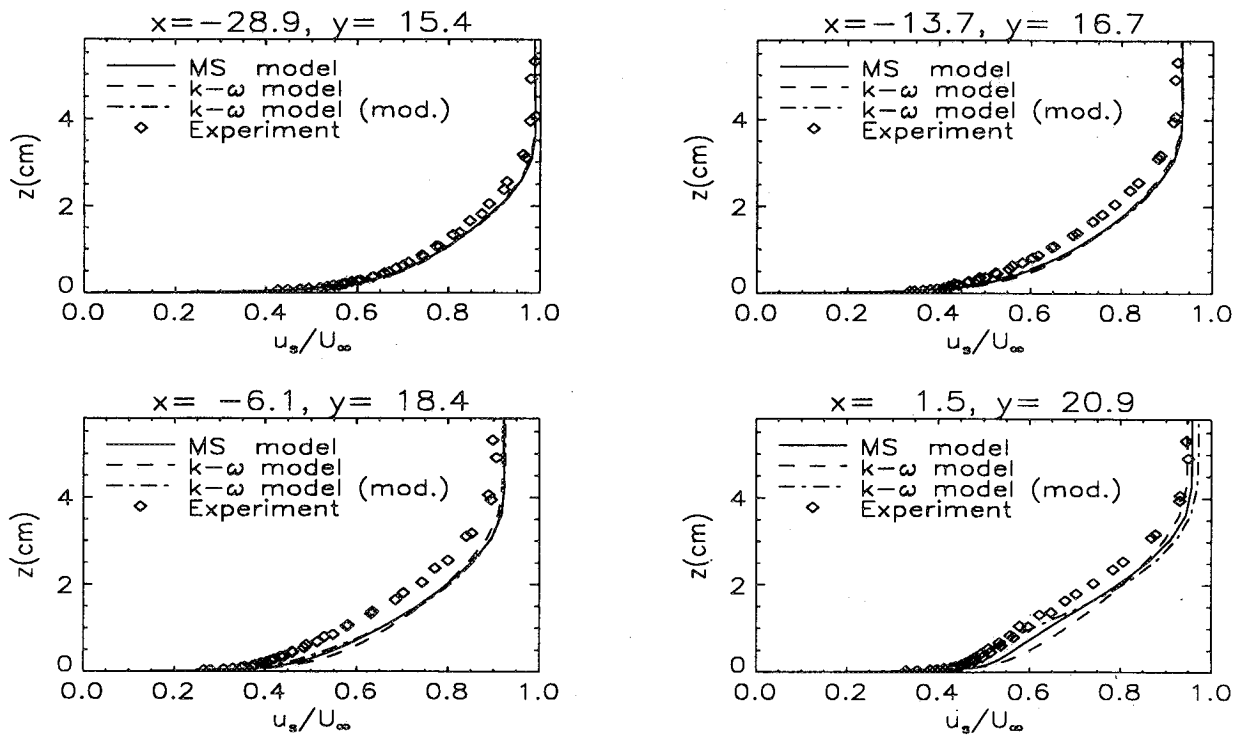

Figure 19. Streamwise velocity profiles along selected streamline for 3D wedge flow.

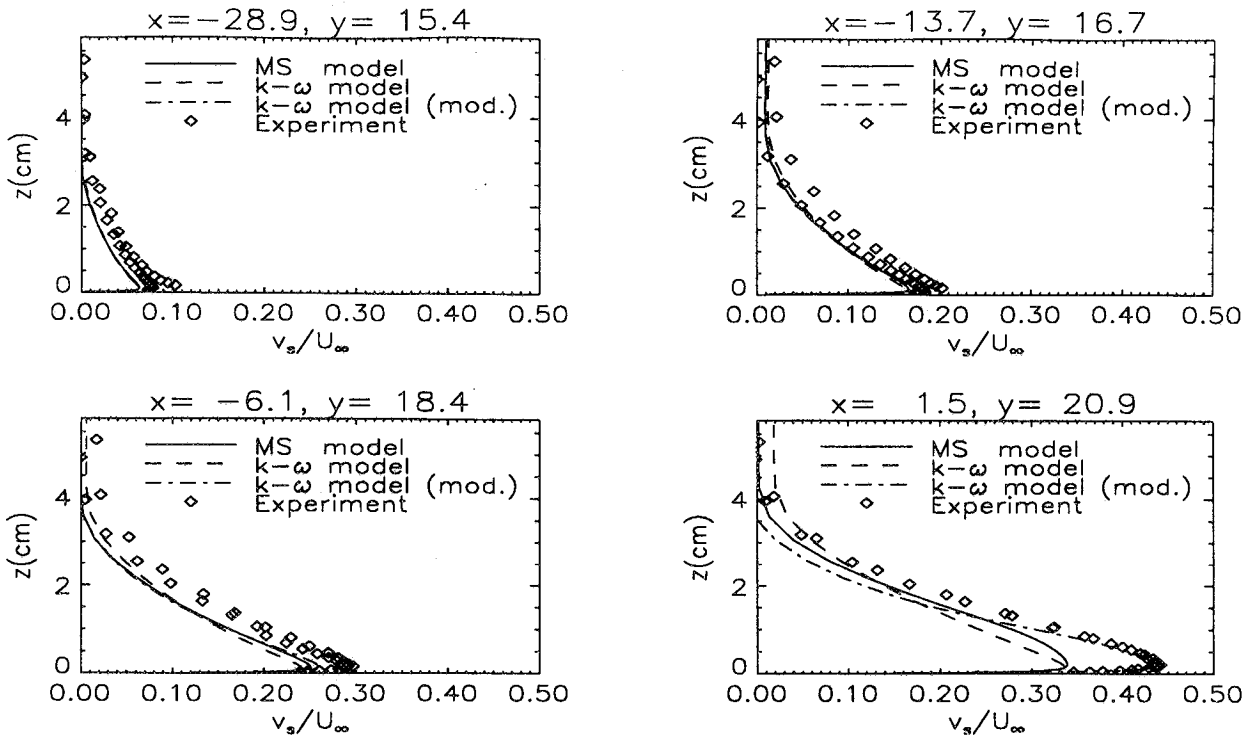

Figure 20. Crossflow velocity profiles along selected streamline for 3D wedge flow.

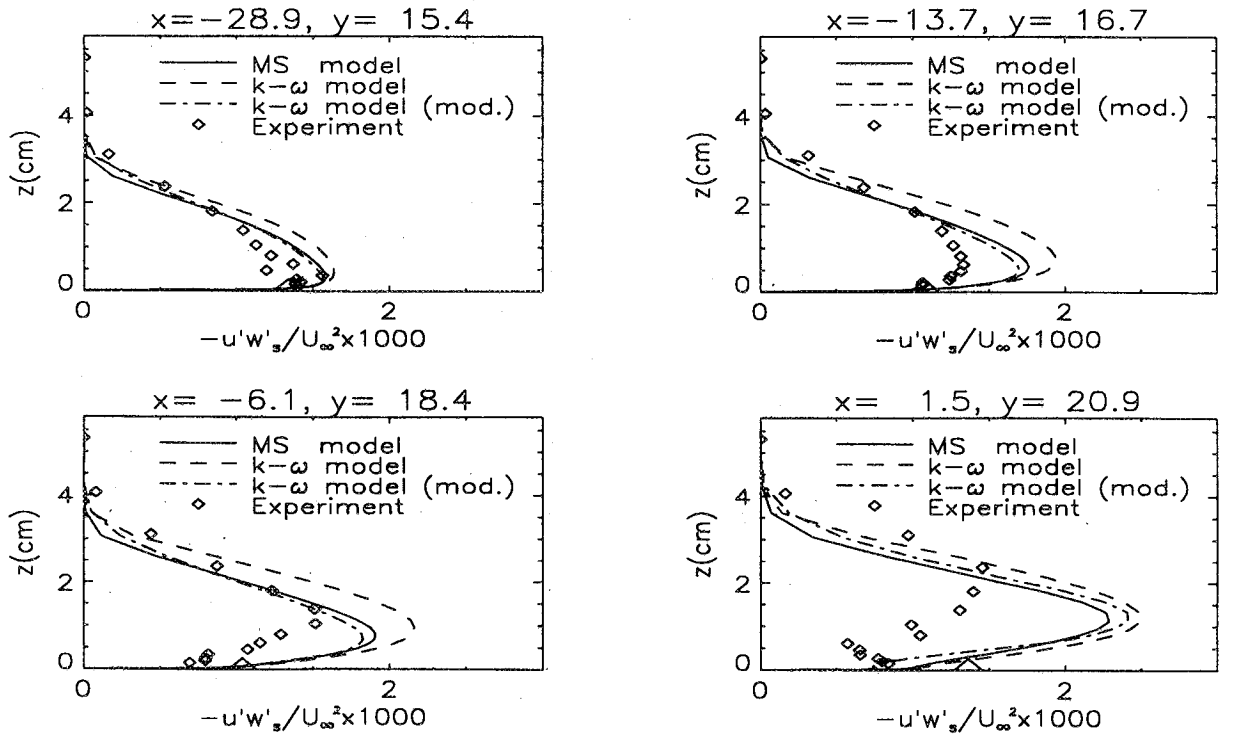

Figure 21. Streamwise shear-stress profiles along selected streamline for 3D wedge flow.

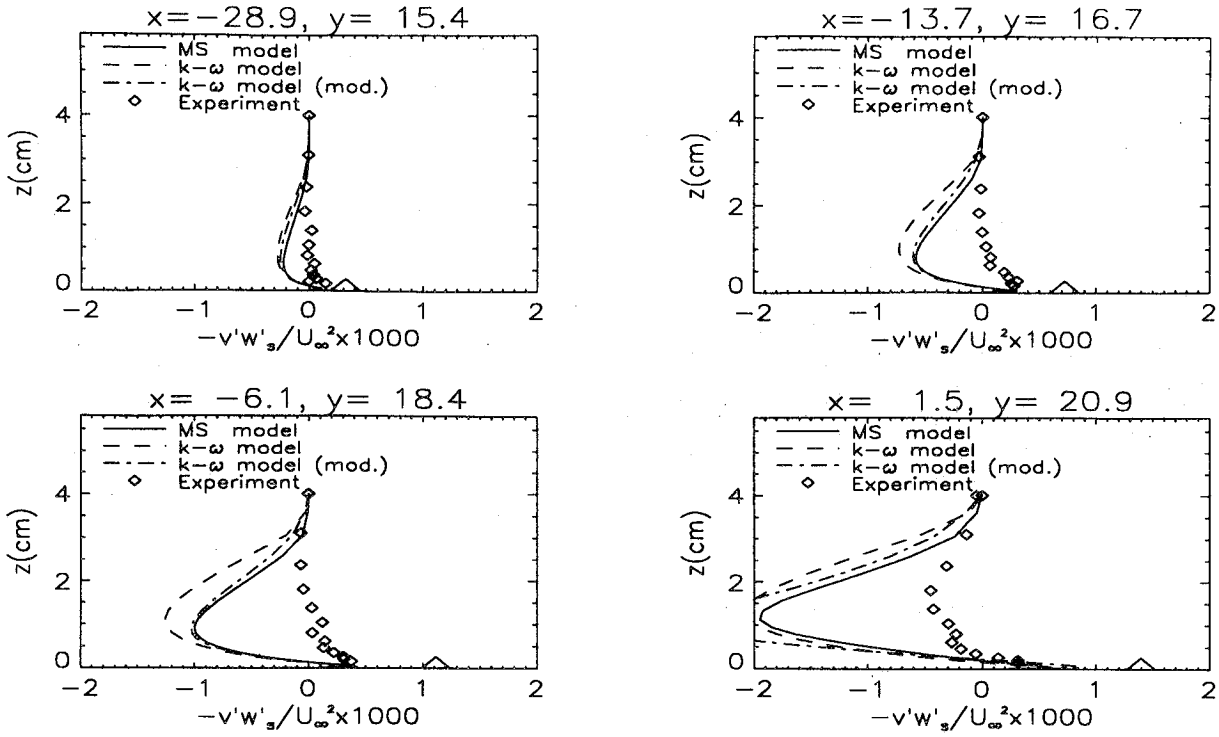

Figure 22. Crossflow shear-stress profiles along selected streamline for 3D wedge flow

potential to give more accurate results, but in practice it is not more successful than the two-equation models.

The above finding that the inclusion of the transport effects improves the prediction of pressure-driven three-dimensional boundary layer computations are in agreement with Kavasaoglu et al. (ref. 20). In their paper the pressure-driven boundary layer flow of Van den Berg and Elsenaar (ref. 21) was computed with different turbulence models. The Johnson-King model (ref. 13) improved the predictions considerably when compared with models that did not account for the transport of the principal shear stress.

CONCLUSIONS

A numerical method has been presented to solve a full Reynolds-stress model in combination with the three-dimensional Navier–Stokes equations. The equations for the Reynolds-stresses are solved decoupled from the mean flow equations with a higher order upwind TVD scheme. The numerical stability of the algorithm is enhanced by retaining the eddy-viscosity formulation and treating the rest of the stresses as explicit source terms.

Computations have been performed for four different flowfields, and the numerical results were compared with solutions based on the $k-\omega$ model in its original form and in a modified version recently proposed by the author. The modified version accounts for the transport effect of the principal shear stress by limiting the eddy-viscosity in a way that keeps the principal shear stress smaller or equal to $0.3k$.

As expected, all three models give accurate predictions for the zero-pressure-gradient flat plate boundary layer.

The computations for the separated adverse pressure gradient flow show a decisive advantage of the MS and the modified $k-\omega$ model due to their ability to properly account for the transport of the shear stresses.

For the spinning cylinder flow, all three models produce rather unsatisfying results. None of the models is able to predict the destabilizing effect of the curvature on the turbulence. While this is to be expected from the eddy-viscosity models, it is also true for the Reynolds-stress model. Obviously, the correct treatment of the production terms is not sufficient to predict this complicated phenomenon.

The last set of computations was performed for a three-dimensional wedge flow. In this flow a strong lateral pressure gradient produces highly skewed velocity profiles. The main challenge of this type of flow is that the shear-stress direction is no longer aligned with the strain-rate direction, and that the skewing of the velocity profiles reduces the shear-stress levels considerably. Both effects are beyond the scope of the eddy-viscosity models, but are also not predicted by the MS model. The success of the modified $k-\omega$ model in predicting the correct amount of crossflow shows, however, that the reduction of the shear stress levels due to the inclusion of the transport terms is at least as important an effect, and gives some hope that this type of flow can be predicted with sufficient accuracy by a comparatively simple model.

In conclusion, the full Reynolds-stress model did not show an advantage over an improved two-equation model for the flows considered in this paper. Its main advantage over standard two-equation models seems to be the ability to account for the transport terms of the turbulent stresses. Obviously, this can also be achieved within the framework of two-equation models. The additional complexity of solving a full Reynolds-stress model does not seem to be justified for the types of flows considered here, unless better models can be developed.

REFERENCES

1. Rogers, S. E.; and Kwak, D.: An Upwind Differencing Scheme for the Time-Accurate Incompressible Navier–Stokes Equations. AIAA Paper 88-2583, Williamsburg, VA, 1988.

2. Wilcox, D. C.: Multiscale Model for Turbulent Flows. AIAA Journal, vol. 26, Nov. 1988, pp. 1311-1320.

3. Launder, B. E.; Reece, G. J.; and Rodi, W.: Progress in the Development of a Reynolds-Stress Turbulence Closure. J. Fluid Mech., vol. 68, part 3, 1975, pp. 537-566.

4. Huang, P. G.; and Leschziner, M. A.: Stabilization of Recirculating Flow Computations with Second-Moment Closures and Third-Order Discretization. Proc. Fifth Turbulent Shear Flows Conference, Cornell University, 1985.

5. Brankovic, A.; and Syed, S.: Validation of Reynolds-Stress Turbulence Model in Generalized Coordinates. AIAA Paper 91-1782, 1991.

6. Chakravarthy, S. R.; and Osher, S.: A New Class of High Accuracy TVD Schemes for Hyperbolic Conservation Laws. AIAA Paper 85-0363, Reno, Nevada, 1985.

7. Driver, D. M.: Reynolds Shear Stress Measurements in a Separated Boundary Layer. AIAA Paper 91-1787, 1991.

8. Driver, D. M.; and Johnston, J. P.: Experimental Study of a Three-Dimensional, Shear-Driven, Turbulent Boundary Layer. NASA TM-102211, Oct. 1989.

9. Driver, D. M.; and Johnston, J. P.: Three-Dimensional Boundary Layer Flow with Streamwise Adverse Pressure Gradient. Proc. Tenth Australian Fluid Mechanics Conference, Dec. 1989.

10. Anderson, S. D.; and Eaton, J. K.: An Experimental Investigation of Pressure Driven Three Dimensional Turbulent Boundary Layers. Report MD-49, Thermoscience Division, Department of Mechanical Engineering, Stanford University, 1987.

11. Menter, F. R.: Performance of Popular Turbulence Models For Attached and Separated Adverse Pressure Gradient Flows. AIAA Paper 91-1784, 1991.

12. Bradshaw, P.; and Pontikos, N.: Measurements in the Turbulent Boundary Layer of an "Infinite" Swept Wing. Journal of Fluid Mech., vol. 159, 1985, pp. 105-130.

13. Johnson, D. A.; and King, L. S.: A Mathematically Simple Turbulence Closure Model for Attached and Separated Turbulent Boundary Layers. AIAA Journal, vol. 23, Nov. 1985, pp. 1684-1692.

14. Vollmers, H.; and Rotta, J. C.: Similar Solutions of the Mean Velocity, Turbulent Energy and Length Scale Equation. AIAA Journal, vol. 15, no. 5, 1977, pp. 714-720.

15. Wilcox, D. C.: Reassessment of the Scale-Determining Equation for Advanced Turbulence Models. AIAA Journal, vol. 26, Nov. 1988, pp. 1299-1310.

16. Menter, F. R.: On the Influence of Freestream Values on the Predictions with the $k-\omega$ Turbulence Model. To be published in the AIAA Journal.

17. Gibson, M. M.; and Younis, B. A.: Calculation of Turbulent Boundary Layers on Curved Surfaces. Phys. Fluids, vol. 24, no. 3, 1981.

18. Irwin, H. P. A.; and Smith, P. A.: Prediction of the Effect of Streamline Curvature on Turbulence. The Physics of Fluids, vol. 18, no. 6, June 1975, pp. 624-630.

19. Lumley, J. L.: Computational Modeling of Turbulent Flows. Advances in Applied Mechanics, vol. 18, Academic Press, NY, pp. 123-176.

20. Kavasaoglu, S. M.; Kaynak, U.; and Van Dalsem, W. R.: Three-Dimensional Application of the Johnson-King Turbulence Model for a Boundary-Layer Direct Method. Computers & Fluids, vol. 19, no. 3/4, 1991, pp. 363-376.

21. Van den Berg, B.; and Elsenaar, A.: Measurements in a Three-Dimensional Incompressible Turbulent Boundary Layer in an Adverse Pressure Gradient Under Infinite Swept Wing Conditions. Report NLR-TR-72092U, 1972.

REPORT DOCUMENTATION PAGE

Form Approved
OMB No. 0704-0188

1. AGENCY USE ONLY *(Leave blank)*	2. REPORT DATE	3. REPORT TYPE AND DATES COVERED
	September 1992	Technical Memorandum

4. TITLE AND SUBTITLE

Assessment of Higher Order Turbulence Models for Complex Two- and Three-Dimensional Flowfields

5. FUNDING NUMBERS

505-59-40

6. AUTHOR(S)

Florian R. Menter (Eloret Institute, Palo Alto, CA)

7. PERFORMING ORGANIZATION NAME(S) AND ADDRESS(ES)

Ames Research Center
Moffett Field, CA 94035-1000

8. PERFORMING ORGANIZATION REPORT NUMBER

A-92124

9. SPONSORING/MONITORING AGENCY NAME(S) AND ADDRESS(ES)

National Aeronautics and Space Administration
Washington, DC 20546-0001

10. SPONSORING/MONITORING AGENCY REPORT NUMBER

NASA TM-103944

11. SUPPLEMENTARY NOTES

Point of Contact: Florian Menter, Ames Research Center, MS 229-1, Moffett Field, CA 94035-1000
(415) 604-6229

12a. DISTRIBUTION/AVAILABILITY STATEMENT

Unclassified — Unlimited
Subject Category 34

12b. DISTRIBUTION CODE

13. ABSTRACT *(Maximum 200 words)*

A numerical method will be presented to solve the three-dimensional Navier–Stokes equations in combination with a full Reynolds-stress turbulence model. Computations will be shown for three complex flowfields. The results of the Reynolds-stress model will be compared with those predicted by two different versions of the $k-\omega$ model. It will be shown that an improved version of the $k-\omega$ model gives as accurate results as the Reynolds-stress model.

14. SUBJECT TERMS

Reynolds-stress model, Navier–Stokes equations, Three-dimensional

15. NUMBER OF PAGES

28

16. PRICE CODE

A03

17. SECURITY CLASSIFICATION OF REPORT	18. SECURITY CLASSIFICATION OF THIS PAGE	19. SECURITY CLASSIFICATION OF ABSTRACT	20. LIMITATION OF ABSTRACT
Unclassified	Unclassified		